INTERNATIONAL JOURNAL FOR NUMERICAL METHODS IN FLUIDS
Int. J. Numer. Meth. Fluids 2008; **57**:1371–1395
Published online 27 March 2008 in Wiley InterScience (www.interscience.wiley.com). DOI: 10.1002/fld.1756

Least-squares spectral element method applied to the Euler equations

Marc Gerritsma[1,*,†], Rokus van der Bas[1], Bart De Maerschalck[2], Barry Koren[1,3] and Herman Deconinck[4]

[1]*Faculty of Aerospace Engineering, Delft University of Technology, Kluyverweg 1, 2629 HS Delft, The Netherlands*
[2]*Flemish Institute for Technological Research, Boeretang 200, 2400 Mol, Belgium*
[3]*Centrum voor Wiskunde en Informatica, Kruislaan 413, 1098 SJ Amsterdam, The Netherlands*
[4]*Von Karman Institute for Fluid Dynamics, Waterloosesteenweg 72, 1640 Sint-Genesius-Rode, Belgium*

SUMMARY

This paper describes the application of the least-squares spectral element method to compressible flow problems. Special attention is paid to the imposition of the weak boundary conditions along curved walls and the influence of the time step on the position and resolution of shocks. The method is described and results are presented for a supersonic flow over a wedge and subsonic, transonic and supersonic flow problems over a bump. Copyright © 2008 John Wiley & Sons, Ltd.

Received 24 September 2007; Revised 18 December 2007; Accepted 18 December 2007

KEY WORDS: spectral element methods; least-squares formulation; Euler equations

1. INTRODUCTION

1.1. Compressible flows

The numerical simulation of inviscid, compressible flow problems has been an active area of research over the past decades. Transonic and supersonic flows admit discontinuous solutions, and a proper numerical setting is required to predict the correct shock location and shock strength. In addition, many compressible flow problems are not well posed in the sense that they do not possess a unique solution. The physical solution—the entropy solution[‡]—is the solution obtained by taking the limit of the (unique) viscous problem for the viscosity tending to zero [1].

*Correspondence to: Marc Gerritsma, Faculty of Aerospace Engineering, Delft University of Technology, Kluyverweg 1, 2629 HS Delft, The Netherlands.
†E-mail: M.I.Gerritsma@TUDelft.nl

‡The entropy condition is a restatement of the vanishing viscosity limit.

This approach is also adopted in nearly all numerical schemes. One adds a certain amount of numerical dissipation to converge to the correct solution. The addition of the dissipative terms, however, serves three quite distinct purposes: First of all, the addition of a small amount of dissipation at the continuous level (prior to any discretization) ensures that we have a unique solution. Secondly, nearly all numerical algorithms require the addition of damping terms to ensure stability; i.e. without the additional damping many schemes will blow up instead of converge. And finally, the additional damping is usually used to suppress any over- and undershoot in the vicinity of large gradients and shocks.

A necessary requirement for numerical schemes is that they are stable and converge to the physical solution. As long as spurious wiggles in the vicinity of discontinuities do not hinder the numerical procedure from converging to a stable solution, there is no need to remove these oscillations *a priori*. Note, in particular, that convergence in a Lebesgue measure does not preclude these oscillations; these oscillations will persist even in the limit. The local oscillations in the limiting solution are known as the Gibbs phenomenon.

Another important feature in compressible flows is the use of a conservative scheme, which means that the conservation laws (mass, momentum and energy) are satisfied at the discrete level. The Rankine–Hugoniot relations that relate discontinuities before and after a shock are essentially a restatement of these conservation laws in the vicinity of the shock. Hence, by employing a conservative scheme many of the continuous relations also hold true at the discrete level. This is the main reason why finite volume methods are so popular in compressible flow dynamics, see for instance [2–4].

The converse is, however, not true: conservative schemes are not necessary to converge to the exact solution. Least-squares formulations are known to suffer from lack of conservation [5–8], and it is therefore rather challenging to apply this weak formulation to problems that contain discontinuous solutions (shocks, contact discontinuities).

1.2. Higher order/spectral

Very little work has been done on inviscid, compressible flow problems in the framework of higher-order/spectral methods. The main reason why so little work has been done in this field using spectral methods is mainly due to the appearance of shocks and contact discontinuities. Spectral methods work best when the coefficients of the higher orthogonal basis functions in the solution decay sufficiently fast [9], in which case exponential convergence to the exact solution may result. The smoothness of the solution dictates the decay rate of the coefficients of the global spectral basis functions, see, for example, Gottlieb and Hesthaven [10]. In case of discontinuous solutions, the coefficients of the higher-order modes decay very slowly and the approximate solution tends to oscillate in the vicinity of large gradients. These wiggles are prone to pollute the entire computational domain. Damping or filtering of these unwanted oscillations is therefore required. The application of spectral methods to non-linear hyperbolic equations has been mainly restricted to one-dimensional model problems, such as the Burgers equation, see, for instance, [11–13] and references therein.

1.3. Least-squares formulation

The least-squares formulation is gaining renewed interest due to some favorable properties. The least-squares formulation often shows optimal convergence, in contrast to the conventional Galerkin approximation which generally yields sub-optimal convergence rates. Furthermore, the

DOI: 10.1002/fld

least-squares formulation is inherently stable and does not require artificial dissipation/viscosity to stabilize the scheme. In addition, a well-posed least-squares approximation always leads to symmetric, positive definite (SPD) systems, which is very convenient from a computational point of view since only half of the system matrix needs to be computed and SPD systems are highly amenable to well-established iterative solvers such as the preconditioned conjugate gradient algorithm.

Despite these attractive features, very little work has been done in the field of linear and non-linear hyperbolic equations. In the least-squares finite element (LSFEM) framework work has been done by Jiang [14]. The techniques investigated by Jiang are as follows:

1. The minimization of the residuals in the L^1-norm, which has recently been addressed by Guermond [15] and Guermond and Popov [16].
2. The iteratively reweighed LSFEM in which the least-squares functional is weighted by the reciprocal of the residual to the power $\kappa > 1$. The effect of this procedure is that regions with high residuals are less emphasized in the minimization of the functional than regions with small residuals.
3. Minimization in the H^1-norm. By minimizing not only the residual but also its gradient in the L^2-norm, oscillations in the solution are suppressed.
4. A conservative formulation in which the fluxes are introduced as additional variables.

De Sterck *et al.* [17, 18] showed that the use of the conservative formulation employed by Jiang is necessary for a proper description of non-linear hyperbolic equations. For the Burgers equation, it is shown that the solution is not in H^1, but the velocity–flux pair (u, f) is a member of $H(\mathrm{div})$. This analysis has been used by De Maerschalck and Heinrichs in the least-squares spectral element context [19–24].

Taghaddosi *et al.* [25, 26] applied the least-squares finite element formulation to the two-dimensional Euler equations in combination with grid adaptation.

For a general overview of the least-squares formulation, the reader is referred to [14, 27] and references therein.

1.4. Outline of this paper

In Section 2, the Euler equations describing an inviscid, compressible flow will be presented in terms of conserved variables (mass, momentum and energy). In Section 3, the weak formulation based on a least-squares approximation is presented. In Section 4, the time-stepping procedure is discussed. A brief description of the spectral method used in this paper is described in Section 5. In Section 6, results will be presented for a flow over a wedge and for subsonic, transonic and supersonic flows in a channel over a circular bump. Concluding remarks are given in Section 7. In Appendix A, the linearized Euler equations are given.

2. COMPRESSIBLE FLOWS

Compressible flows in the absence of dissipative terms are governed by the Euler equations. There are several ways in which the Euler equations in differential form can be written, but only the conservative form in terms of conservation quantities will be presented.

DOI: 10.1002/fld

The two-dimensional Euler equations in conservation form are given by

$$\frac{\partial}{\partial t}\begin{bmatrix}\rho\\ \rho u\\ \rho v\\ \rho E\end{bmatrix}+\frac{\partial}{\partial x}\begin{bmatrix}\rho u\\ \rho u^2+p\\ \rho uv\\ \rho uH\end{bmatrix}+\frac{\partial}{\partial y}\begin{bmatrix}\rho v\\ \rho uv\\ \rho v^2+p\\ \rho vH\end{bmatrix}=\begin{bmatrix}0\\ 0\\ 0\\ 0\end{bmatrix} \tag{1}$$

These equations express conservation of mass, conservation of momentum in the x- and y-directions and conservation of energy, respectively. Here ρ is the local density, p is the pressure and (u, v) denotes the fluid velocity. The total energy per unit mass is denoted by E. The total energy can be decomposed into internal energy e and the kinetic energy per unit mass

$$\rho E=\rho e+\frac{\rho}{2}(u^2+v^2)=\frac{p}{\gamma-1}+\frac{\rho}{2}(u^2+v^2) \tag{2}$$

where in the last equality we assume a calorically ideal, perfect gas. The total enthalpy, H, is defined as

$$H=E+\frac{p}{\rho} \tag{3}$$

For steady flows, the enthalpy is constant along the streamlines.

If the spatial fluxes depend continuously on the conserved quantities $\mathbf{u}=(\rho, \rho u, \rho v, \rho E)^{\mathrm{T}}$, we can express the governing equation in non-conservative form as

$$\mathbf{u}_{\mathrm{t}}+A(\mathbf{u})\mathbf{u}_x+B(\mathbf{u})\mathbf{u}_y=\mathbf{0} \tag{4}$$

where $A(\mathbf{u})$ and $B(\mathbf{u})$ are the Jacobian matrices, given in Appendix A.

An alternative formulation is obtained by writing the governing equations in terms of the primitive variables $\mathbf{u}=(\rho, u, v, p)^{\mathrm{T}}$. However, application of this formulation to test problems for which analytic solutions are available shows that this formulation introduces errors in the shock position and the least-squares method converges to the wrong solution [28]. An example of such errors will be given in Section 6.1. Therefore, in this paper only the Euler equations in terms of the conserved variables will be considered.

3. THE LEAST-SQUARES FORMULATION

The least-squares formulation is based on the equivalence of the residual in a certain norm and the error in an associated norm. If this equivalence is established, one aims to minimize the residual norm which then provides an upper bound for the error in the associated norm.

In order to explain the method, consider the abstract differential equation given by

$$\mathscr{L}u=f, \quad x\in\Omega \tag{5}$$

with

$$\mathscr{R}u=g, \quad x\in\Gamma\subset\partial\Omega \tag{6}$$

DOI: 10.1002/fld

Here $\mathscr{L}$ denotes a linear (or linearized) partial differential operator, which for the linearized Euler equations is given in Appendix A (see also [28]). $\mathscr{R}$ denotes a linear trace operator by which Dirichlet boundary conditions are prescribed. The data f and g are known vectors. Without loss of generality, we can set $g=0$.

If the problem is well posed, the operator $(\mathscr{L},\mathscr{R})$ will be a continuous mapping from the underlying Hilbert space $X=X(\Omega)$ onto the Hilbert spaces $Y=Y(\Omega)$ and $Z=Z(\Gamma)$, with a continuous inverse. Here $\Gamma\subset\partial\Omega$ is the part of the boundary where boundary conditions are prescribed. This can be expressed by the following inequalities:

$$C_1\|u\|_X\leqslant\|\mathscr{L}u\|_Y+\|\mathscr{R}u\|_Z\leqslant C_2\|u\|_X,\quad\forall u\in X \tag{7}$$

These inequalities establish norm equivalence between the residuals and the error. We assume that the exact solution $u_{\text{ex}}\in X$, then by the linearity of $\mathscr{L}$ and $\mathscr{R}$ we have

$$C_1\|u-u_{\text{ex}}\|_X\leqslant\|\mathscr{L}u-f\|_Y+\|\mathscr{R}u-g\|_Z\leqslant C_2\|u-u_{\text{ex}}\|_X,\quad\forall u\in X \tag{8}$$

These inequalities state that if the residuals of the differential equation measured in the Y-norm and the traces measured in the Z-norm go to zero, the exact solution is approximated in the X-norm. On the basis of this observation, we introduce the least-squares functional

$$\mathscr{I}(u)=\tfrac{1}{2}(\|\mathscr{L}u-f\|_Y^2+\|\mathscr{R}u-g\|_Z^2),\quad\forall u\in X \tag{9}$$

Minimization of this functional with respect to u gives the weak formulation

$$(\mathscr{L}u,\mathscr{L}v)_Y+W(\mathscr{R}u,\mathscr{R}v)_Z=(f,\mathscr{L}v)_Y+W(g,\mathscr{R}v)_Z,\quad\forall v\in X \tag{10}$$

Generally, the least-squares method is applied to overdetermined systems where one has more equations than unknowns, see, for instance, [29]. The least-squares solution is the solution that minimizes the residual in the L^2-norm. By adding weights larger than one to some of the equations, one can force the solution to reduce the residual for that particular equation. By taking a weight smaller than one, one allows the residual of these particular equations to become larger. Here a weighing factor W is inserted for the boundary terms, which allows one to increase or decrease the contribution of the boundary residuals to the overall residual norm. In case the trial solution satisfies the condition $\mathscr{R}u=0$, the boundary terms vanish from the weak formulation.

For numerical calculations, we need to restrict the infinite-dimensional space X to a finite-dimensional subspace, denoted by $X^h\subset X$. Here h denotes a generic discretization parameter, which in this paper will refer to the mesh size or the polynomial degree used in the approximation.

There are two issues that make the application of the least-squares formulation less straightforward when applied to transonic and supersonic inviscid flow calculations. The first point concerns uniqueness and norm equivalence. In the Introduction, it was already mentioned that the Euler equations allow for non-unique solutions; hence, assume that u_{ex}^1 and u_{ex}^2 are two such solutions, then norm equivalence would imply that $\|u_{\text{ex}}^1-u_{\text{ex}}^2\|_X=0$, i.e. $u_{\text{ex}}^1(x)=u_{\text{ex}}^2(x)$ almost everywhere. These two solutions can only differ on a set of measure zero, whereas we know that the Euler equations allow for solutions that differ much more than that. Therefore, we can conclude that norm equivalence cannot hold for the Euler equations. De Maerschalck tried to resolve this non-uniqueness by incorporating the entropy inequality in the least-squares formulation [19]. The entropy condition is obtained by defining an entropy variable and taking the compressible Navier–Stokes equations with vanishing dissipative terms, see, for instance, Tadmor [30] or the lecture notes on entropy and partial differential equations (PDEs) by Evans [31]. The non-uniqueness

DOI: 10.1002/fld

problem is associated with the first inequality in (7); there is no $C_1>0$ for which this inequality holds.

The second issue concerns the second inequality in (7) when we take $Y(\Omega)=L^2(\Omega)$. The second inequality can then be satisfied when $X(\Omega)=H^1(\Omega)$, but for transonic and supersonic flows which contain shocks $u_{\text{ex}}\notin H^1(\Omega)$. A shock is typically modeled as a discontinuous function the derivative of which is a Dirac delta distribution which is not in $L^2(\Omega)$. Hence, the original discontinuous function is not in $H^1(\Omega)$. As a result of the fact that the exact solution is not a member of the functional space $X=H^1$, the residual norm will increase upon mesh refinement. This phenomenon was described by De Sterck *et al.* [18] and numerically reported by De Maerschalck for both *h*- and *p*-refinements [22]. This phenomenon is also known under the name of *Lavrentiev phenomenon*, see, for instance, [32].

Both issues—lack of coercivity and approximability—can be circumvented by considering a regularized problem in which a certain amount of numerical dissipation is added to the governing equations. These additional dissipative terms are incorporated through the time-stepping procedure which will be explained in the following section.

4. TIME INTEGRATION

To iterate towards a steady-state solution a fully implicit backward Euler scheme is employed:

$$\frac{\partial\phi}{\partial t}+\frac{\partial f(\phi)}{\partial x}\approx\frac{\phi^{n+1}-\phi^n}{\Delta t}+\frac{\partial f(\phi^{n+1})}{\partial x} \tag{11}$$

Steady state is declared when $|\phi^{n+1}-\phi^n|/\Delta t\leqslant\text{tol}$, for a given tolerance. This particular choice of time stepping adds numerical dissipation to the scheme and modifies the convection speeds in the problem. This can be seen by considering the following hyperbolic sample problem.

Suppose that we wish to discretize the hyperbolic equation

$$\frac{\partial\phi}{\partial t}+\frac{\partial\phi^b}{\partial x}=0,\quad b\in\mathbb{N}\backslash\{0\} \tag{12}$$

If we apply a high-order spectral element method to the spatial derivatives and backward Euler for the time derivative, the dominant term in the truncation error is due to the time stepping

$$\frac{\partial\phi}{\partial t}+\frac{\partial\phi^b}{\partial x}\approx\frac{\phi^{n+1}-\phi^n}{\Delta t}+\frac{\partial\phi^b}{\partial x} \tag{13}$$

Now

$$\frac{\phi^{n+1}-\phi^n}{\Delta t}=\left.\frac{\partial\phi}{\partial t}\right|_{t=t^{n+1}}-\frac{\Delta t}{2}\left.\frac{\partial^2\phi}{\partial t^2}\right|_{t=t^{n+1}}+O(\Delta t^2) \tag{14}$$

If we approximate the differential equation we have that

$$\frac{\partial^2\phi}{\partial t^2}=\frac{\partial}{\partial t}\left\{\frac{\partial\phi}{\partial t}\right\}\approx\frac{\partial}{\partial t}\left\{-\frac{\partial\phi^b}{\partial x}\right\}=-b\frac{\partial\phi^{b-1}}{\partial t}\frac{\partial\phi}{\partial x}-b\phi^{b-1}\frac{\partial^2\phi}{\partial t\partial x} \tag{15}$$

DOI: 10.1002/fld

This term can be rewritten as

$$-b\frac{\partial\phi^{b-1}}{\partial t}\frac{\partial\phi}{\partial x}-b\phi^{b-1}\frac{\partial^2\phi}{\partial t\partial x}\approx b(b-1)\phi^{b-2}\frac{\partial\phi^b}{\partial x}\frac{\partial\phi}{\partial x}-b\phi^{b-1}\frac{\partial}{\partial x}\left\{-\frac{\partial\phi^b}{\partial x}\right\}$$

$$=b^2(b-1)\phi^{2b-3}\frac{\partial\phi}{\partial x}\frac{\partial\phi}{\partial x}+b^2\phi^{2b-2}\frac{\partial^2\phi}{\partial x^2} \tag{16}$$

Hence, we have that

$$\frac{\partial^2\phi}{\partial t^2}\approx b^2(b-1)\phi^{2b-3}\left(\frac{\partial\phi}{\partial x}\right)^2+b^2\phi^{2b-2}\frac{\partial^2\phi}{\partial x^2} \tag{17}$$

We can therefore express the equivalent differential equation as

$$\frac{\partial\phi}{\partial t}+\left\{b\phi^{b-1}-\frac{\Delta t}{2}b^2(b-1)\phi^{2b-3}\frac{\partial\phi}{\partial x}\right\}\frac{\partial\phi}{\partial x}=\frac{\Delta t}{2}b^2\phi^{2b-2}\frac{\partial^2\phi}{\partial x^2} \tag{18}$$

Hence, we see that backward Euler modifies the advection speed if $b\geqslant 2$ and introduces a certain amount of dissipation for $b\geqslant 1$. These effects have been confirmed by Oldenziel [33], for the Burgers equation ($b=2$) and a highly non-linear conservation law ($b=5$). The dissipative term ensures that we converge to the entropy solution and suppresses oscillations in the vicinity of shocks and contact discontinuities. However, the modified advection speeds may lead to incorrect shock positions and shock strengths. The time step has to be chosen sufficiently large to provide the required stabilization, and sufficiently small to converge to the correct solution. The amount of dissipation in the final solution can be checked by looking at the entropy distribution, $s=p\rho^{-\gamma}$, which should be constant over the entire domain except at shocks, where due to irreversible processes in the shock the entropy should increase.

5. SPECTRAL ELEMENTS

Instead of seeking the minimizer over the infinite-dimensional space X we restrict our search to a conforming subspace $X^h\subset X$ by performing a domain decomposition where the solution within each sub-domain is expanded with respect to a polynomial basis. The domain Ω is sub-divided into K non-overlapping quadrilateral sub-domains Ω^k:

$$\Omega=\bigcup_{k=1}^{K}\Omega^k,\quad \overset{\circ}{\Omega}{}^k\cap\overset{\circ}{\Omega}{}^l=\emptyset,\quad k\neq l \tag{19}$$

Each sub-domain is mapped onto the unit cube $[-1,1]^d$, where $d=\dim(\Omega)$. Within this unit cube the unknown function is approximated by polynomials. In this paper a spectral element method based on *Legendre* polynomials, $L_k(x)$ over the interval $[-1,1]$, is employed [34–36]. We define the Gauss–Lobatto–Legendre (GLL) nodes by the zeros of the polynomial

$$(1-x^2)L'_N(x) \tag{20}$$

DOI: 10.1002/fld

and the Lagrange polynomials, $h_i(x)$, through these GLL points, x_i, by

$$h_i(x)=\frac{1}{N(N+1)}\frac{(x^2-1)L'_N(x)}{L_N(x_i)(x-x_i)} \quad \text{for} \quad i=0,\ldots,N \tag{21}$$

where $L'_N(x)$ denotes the derivative of the Nth Legendre polynomial. For multi-dimensional problems, tensor products of the one-dimensional basis functions are employed in the expansion of the approximate solution. We can therefore expand the approximate solution in each sub-domain in terms of a truncated series of these Lagrangian basis functions, which for $d=2$ yields

$$u^N(x,y)=\sum_{i=0}^{N}\sum_{j=0}^{N}\hat{u}_{ij}h_i(x)h_j(y) \tag{22}$$

where the $\hat{u}_{ij}$'s are to be determined by the least-squares method. Since we have converted a general higher-order PDE to an equivalent first-order system, C^0-continuity suffices to patch the solutions on the individual sub-domains together.

The integrals appearing in the least-squares formulation, (10), are approximated by Gauss–Lobatto quadrature

$$\int_{-1}^{1} f(x)\,\mathrm{d}x \approx \sum_{i=0}^{P} f(x_i)w_i \tag{23}$$

where w_i are the GL weights given by

$$w_i=\frac{2}{P(P+1)}\frac{1}{L_P^2(x_i)}, \quad i=0,\ldots,P\geqslant N \tag{24}$$

It has been shown in [37] that it is beneficial for non-linear equations possessing large gradients to choose the integration order P higher than the approximation of the solution, N.

6. RESULTS

In this section, two test cases will be discussed. This first test case is a supersonic flow over a wedge for which the exact shock position and strength are known analytically. The second test problem is the compressible flow over a circular bottom bump. All calculations were run with a specific heat ratio of $\gamma=1.4$ based on the scaled specific heats of $c_p=1.4$ and $c_v=1$.

6.1. Supersonic flow over a wedge

This test case consists of a two-dimensional channel flow over a wedge which has an angle of 5° starting at $x=1$. A sketch of the geometry can be seen in Figure 1.

At the inflow boundary ($x=0$), the flow is parallel to the x-axis and the flow properties are given by $\rho=1.4$, $p=1$ and $M=2$. An inviscid slip boundary is used for the upper and lower walls of the channel. Since the outflow is supersonic, no boundary conditions are applied at the outflow boundary. The solution for the flow behind the shock is $\rho\approx 1.702$ and $M\approx 1.821$. The angle of the induced shock with the free stream is $\beta\approx 34.3°$.

Taking a 4×3 mesh and using a time step of $\Delta t=0.2$, the solution to the Euler equations is calculated for several polynomial degrees. Figure 2 shows a close-up of the density ρ at the

DOI: 10.1002/fld

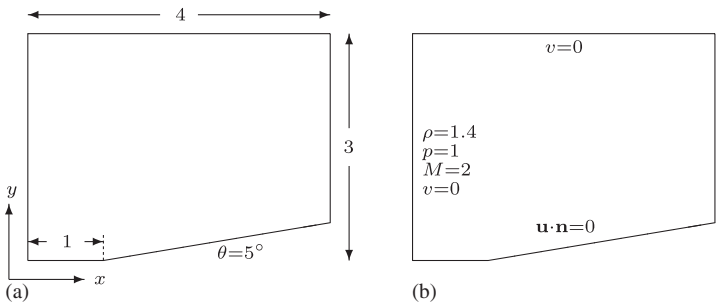

Figure 1. The geometry (a) and the boundary conditions (b) used for flow over wedge.

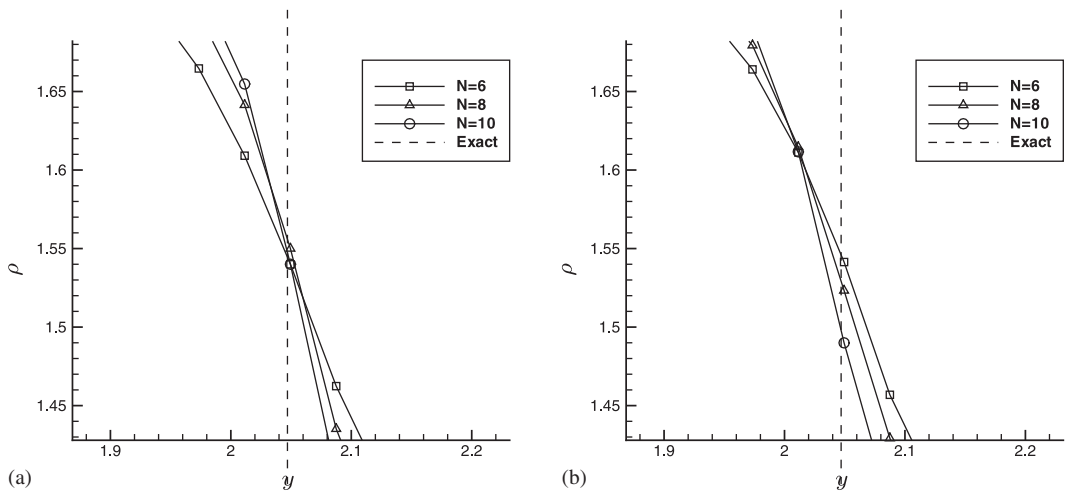

Figure 2. Close-up of the density ρ in vicinity of the exact shock position for different polynomial orders: (a) conserved variables and (b) primitive variables.

outlet boundary in the vicinity of the shock for both primitive and conserved variables for several polynomial degrees. In the conservative-variable case, the shock converges to the correct solution. In the primitive-variable case, it does not. This is illustrated in Figure 2.

6.1.1. p-Convergence. The p-convergence study is conducted using a constant time step $\Delta t = 0.2$ on a 4×3 mesh. Figure 3 shows the density ρ at the outlet boundary, $x = 4$, for different polynomial degrees. As the polynomial degree increases, the shock is resolved more sharply and the gradient of the numerical solution steepens. The strength of the shock seems to be equal to that of the exact solution.

Figure 4 shows the residual and the errors in the L^2-norm. The residual in the L^2-norm increases as the polynomial degree increases. This is a result of the fact that the exact residual is not square integrable and therefore the residual norm should diverge as we approximate the exact solution, see Section 3 for an explanation of this phenomenon. The errors for each variable decrease in the

DOI: 10.1002/fld

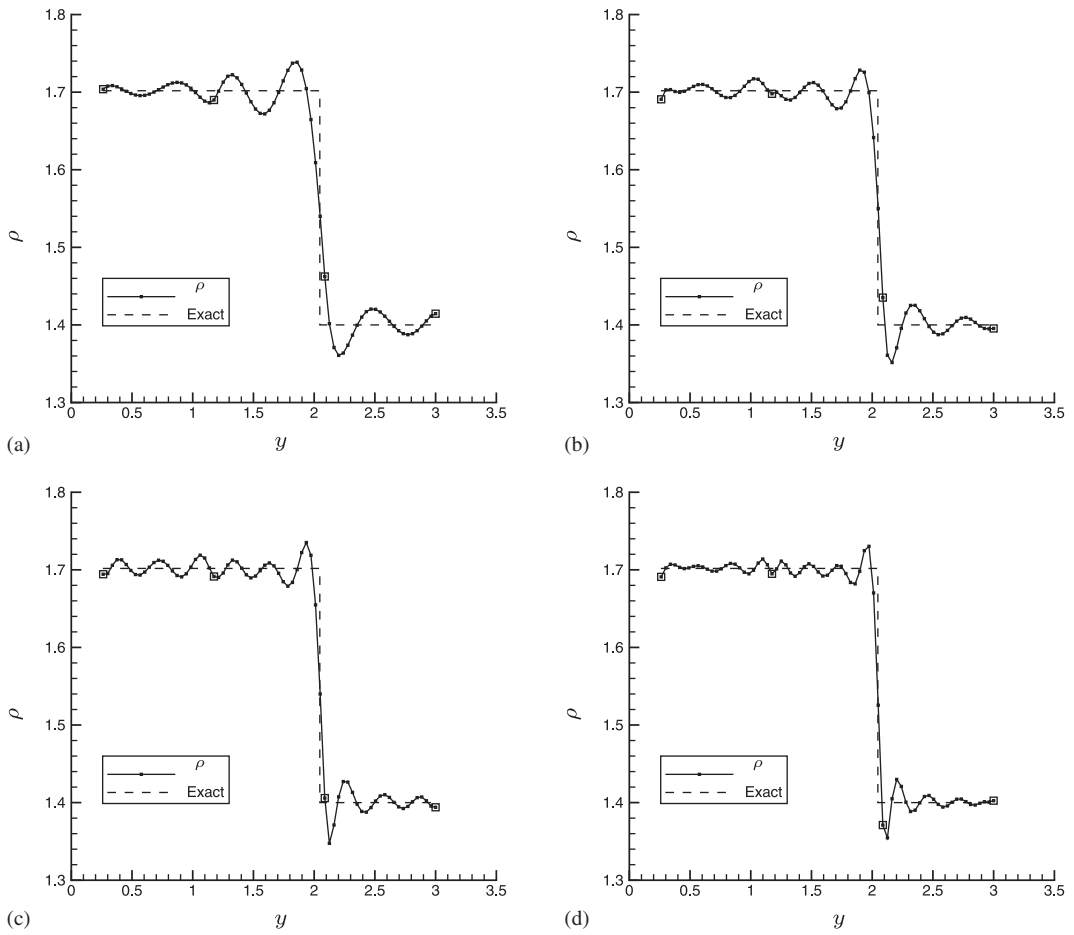

Figure 3. The density at the outlet boundary for the p-convergence on a 4×3 mesh using $\Delta t=0.2$: (a) $P=6$; (b) $P=8$; (c) $P=10$; and (d) $P=12$.

L^2-norm as the polynomial degree increases. Note that the error only decreases algebraically due to the limited regularity of the exact solution.

6.1.2. h-Convergence. For this test case, the h-convergence study has been conducted at a constant time step, $\Delta t=0.2$. Starting from a 4×3 mesh, the number of elements is increased to 108 on a 12×9 mesh using a polynomial degree $N=4$. The integration order is chosen equal to the polynomial order. Figure 5 shows the density at the outlet boundary, $x=4$, for different meshes. Although the oscillations pollute the entire outflow, the oscillatory behavior is generally much more local than the Galerkin methods, see, for instance, [20].

The residual and the errors in the L^2-norm are shown in Figure 6. The residual norm increases as the number of elements increases as explained in Section 3. The rate of convergence as a function of the degrees of freedom is governed by the smoothness of the exact solution and is therefore

DOI: 10.1002/fld

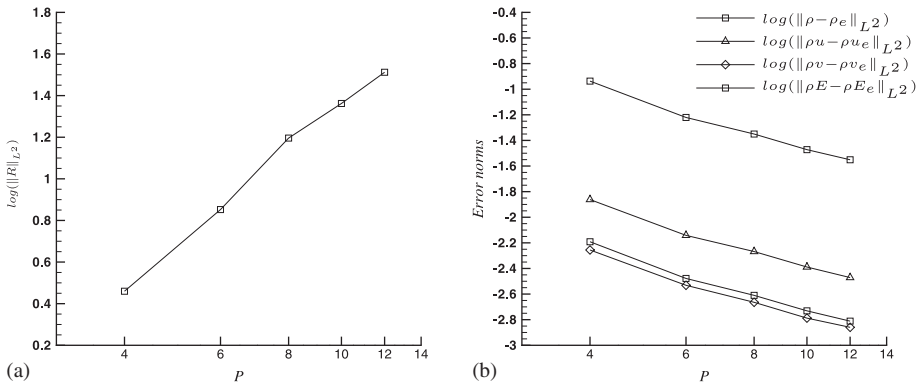

Figure 4. Residuals (a) and errors (b) in the L^2-norm of the p-convergence on a 12-element mesh using a time step of $\Delta t = 0.2$.

equal to the rate of convergence found with p-refinement. By rate of convergence, we mean the L^2-norm of the error as a function of the number of degrees of freedom.

6.2. *Compressible flow over a circular bump*

In this section, results are given for the flow over a circular bump in a two-dimensional channel. Results will be given for subsonic flow, $M_\infty = 0.5$, transonic flow, $M_\infty = 0.85$ and supersonic flow, $M_\infty = 1.4$. This is a difficult test problem over the entire Mach range for spectral methods due to the presence of stagnation points at the leading and trailing edge of the bump.

6.2.1. General geometry and boundary conditions. The general geometry for the channel flow with a circular bump is shown in Figure 7. The bump is modeled by curved elements using the transfinite mapping by Gordon and Hall [38]. In the transfinite mapping, all sides of the quadrilateral element are parameterized

$$\mathbf{x}_\mathrm{b}(\xi), \quad \mathbf{x}_\mathrm{t}(\xi), \quad -1 \leqslant \xi \leqslant 1, \quad \mathbf{x}_\mathrm{l}(\eta), \quad \mathbf{x}_\mathrm{r}(\eta), \quad -1 \leqslant \eta \leqslant 1$$

where the subscripts b, t, l and r refer to the *bottom*, *top*, *left* and *right* boundaries in the logical domain $(\xi, \eta) \in [-1, 1]^2$, respectively.

The transfinite mapping is then given by

$$\begin{aligned}\mathbf{x}(\xi,\eta) = {} & (1-\eta)\mathbf{x}_\mathrm{b}(\xi) + \eta\mathbf{x}_\mathrm{t}(\xi) + (1-\xi)\mathbf{x}_\mathrm{l}(\eta) + \xi\mathbf{x}_\mathrm{r}(\eta) \\ & -\{\xi\eta\mathbf{x}_\mathrm{t}(1) + \xi(1-\eta)\mathbf{x}_\mathrm{b}(1) \\ & +\eta(1-\xi)\mathbf{x}_\mathrm{t}(0) + (1-\xi)(1-\eta)\mathbf{x}_\mathrm{b}(0)\} \end{aligned} \tag{25}$$

In this paper, for the parameterizations for the sides only straight lines and circular arcs are used. All length and height parameters of the channel will be scaled to the chord length c of the bump.

Uniform inflow conditions will be applied and along all walls the normal velocity will be set to zero. At the bump, the normal velocity is weakly imposed, see (10). All other boundary conditions are imposed strongly.

DOI: 10.1002/fld

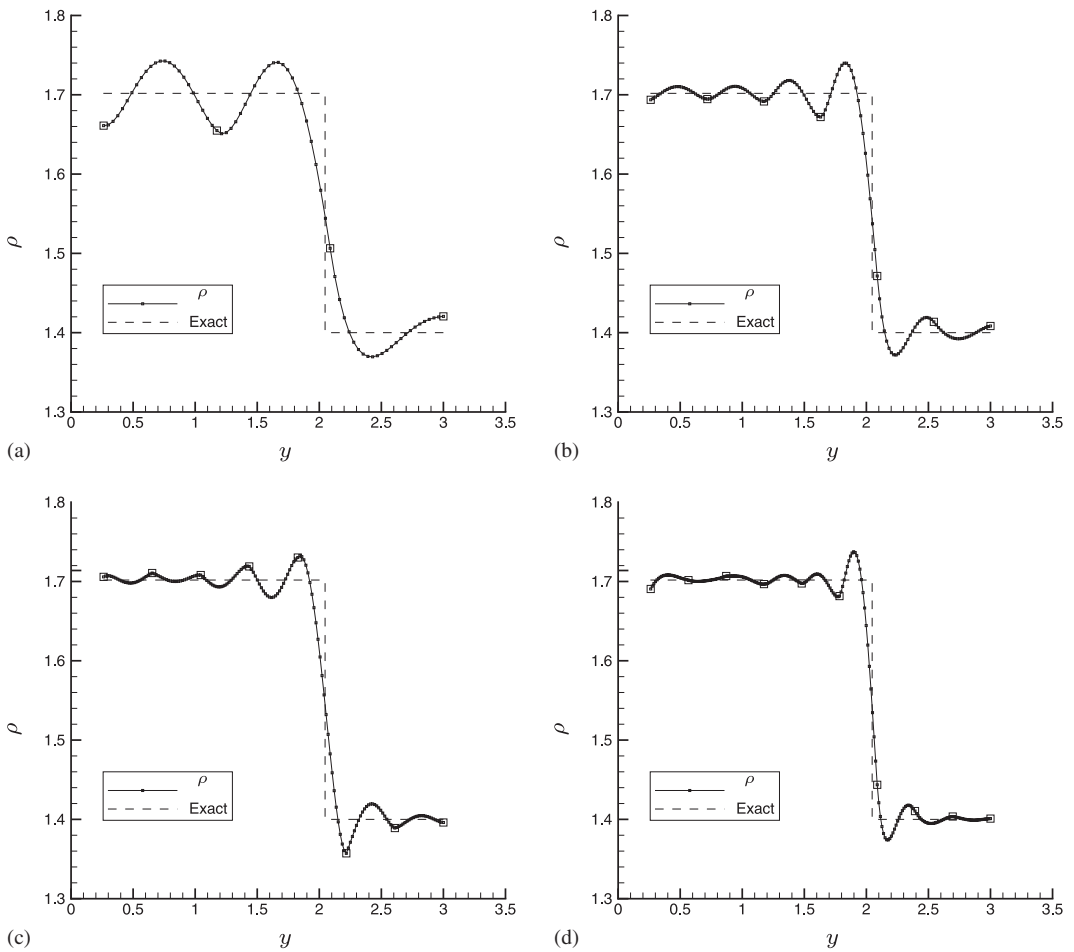

Figure 5. The density at the outlet boundary for the h-convergence, $\Delta t = 0.2$: (a) 12 elements; (b) 48 elements; (c) 70 elements; and (d) 108 elements.

The entropy variation s in the domain is calculated with the freestream entropy as a reference:

$$s = \frac{\hat{s} - \hat{s}_\infty}{\hat{s}_\infty}, \quad \text{where } \hat{s} = p\rho^{-\gamma} \tag{26}$$

6.2.2. Results for subsonic flow. The solution to the subsonic flow problem will not contain shocks, which allows us to assess the influence of the time step, the weighing of the weak boundaries and the mesh on the resolution of the stagnation points at the leading and the trailing edges of the bump.

To test a subsonic flow problem, the chord length of the bump is set at $c = 1$. The length of the channel is three times the chord length, whereas the height is set equal to the chord length. The height of bump is 10% of the chord length. The mesh contains 33 elements (Figure 8) and

DOI: 10.1002/fld

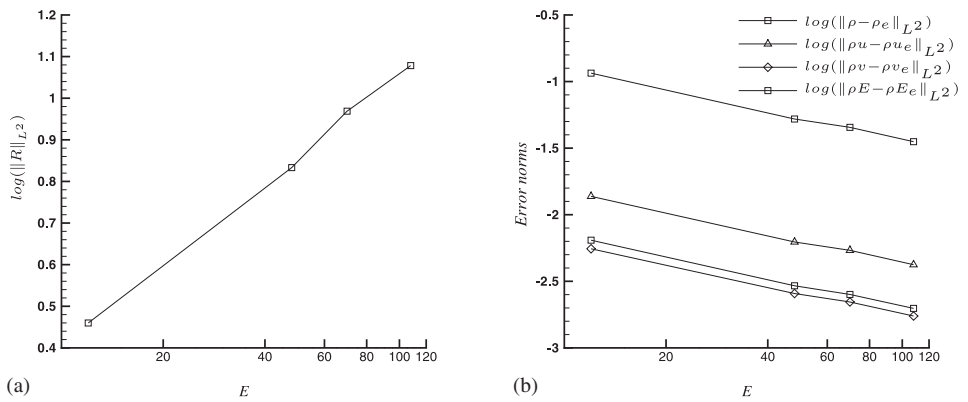

Figure 6. Residuals (a) and errors (b) in the L^2-norm for the h-convergence.

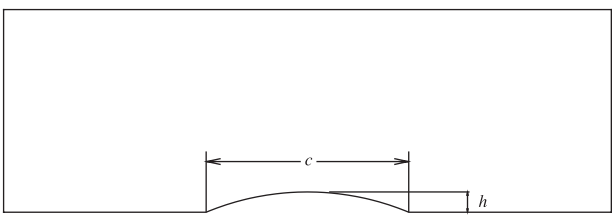

Figure 7. The general geometry of the two-dimensional channel with a circular bump.

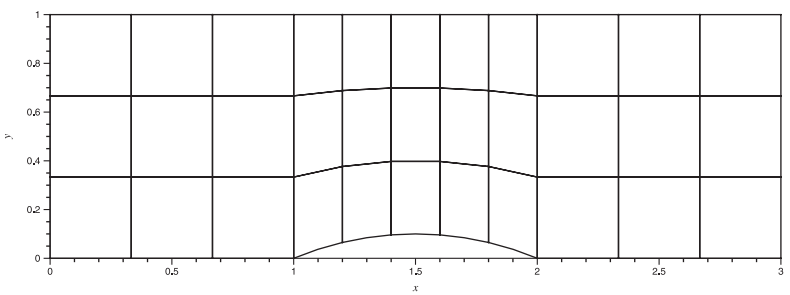

Figure 8. The mesh used for the subsonic test case. The height of the bump is 10% of the chord length and 33 elements are used.

the polynomial degree chosen is $N=6$. An integration order $P=8$ is chosen, see (23). De Maerschalck and Gerritsma [37] demonstrated that over-integration is beneficial for non-smooth problems to account for the slowly decaying higher-order modes in the system.

At the outflow boundary, the exit pressure is set at $p=1$. At the inflow boundary, the density is prescribed and set at $\rho=1.4$; the velocity components are fixed at $u=0.5$ and $v=0$.

Figure 9 shows the influence of the time step on the Mach number along the lower wall.

DOI: 10.1002/fld

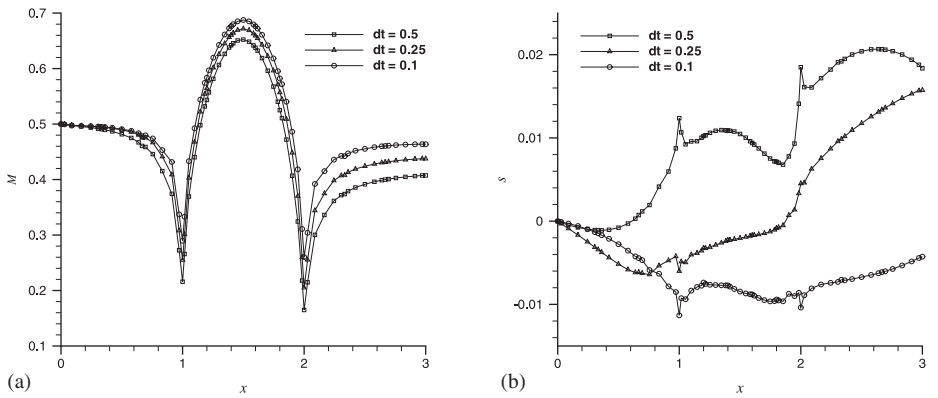

Figure 9. (a) The Mach number and (b) entropy distribution for the subsonic flow and boundary weight $W = 1$ for different time steps.

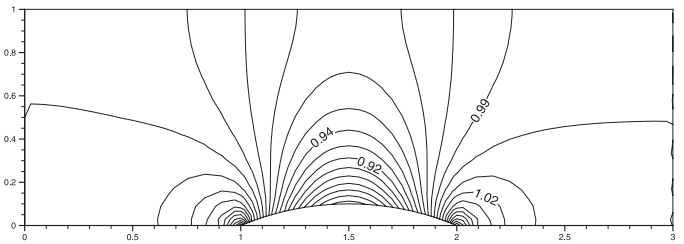

Figure 10. Pressure contours for the subsonic flow with boundary weight $W = 1$ and $\Delta t = 0.1$.

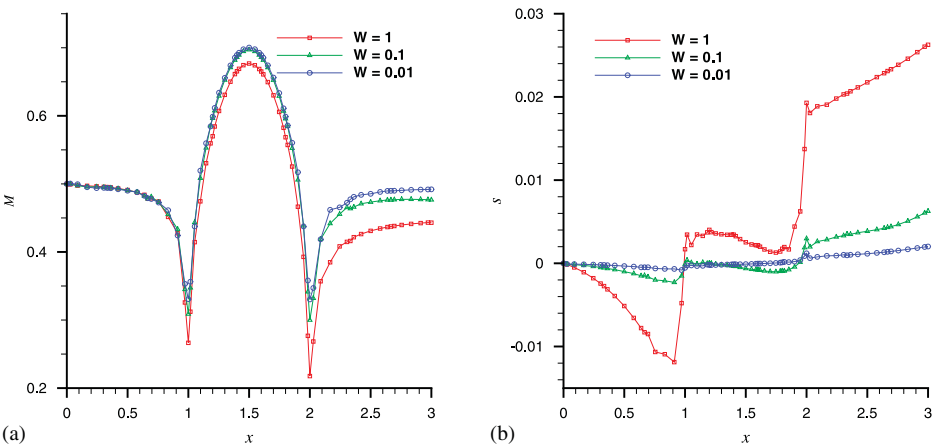

Figure 11. (a) The Mach number and (b) entropy distribution for the subsonic flow using different boundary weights for $\Delta t = 0.1$.

DOI: 10.1002/fld

We see that if the time step is reduced, the artificial diffusion also becomes smaller yielding higher Mach number at the crest of the bump. The change in entropy reduces from 2% for $\Delta t = 0.5$ to 1% for $\Delta t = 0.1$. Pressure contours are given in Figure 10.

Figure 11 shows the influence of the weighing factor W, (10), on the Mach number and entropy distributions along the lower wall for $\Delta t = 0.1$.

The influence of the mesh is assessed by refining the mesh around the stagnation point. The refined mesh consists of 72 elements, Figure 12. The results for a polynomial degree $N = 4$, integration order $P = 5$, time step $\Delta t = 0.05$ and weight factor $W = 1$ along the lower wall are displayed in Figure 13. This figure shows that the resolution of the stagnation points is more

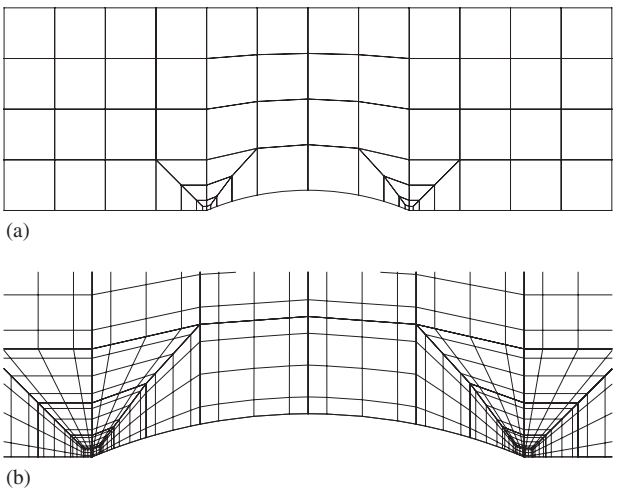

Figure 12. Refined mesh near stagnation points consisting of 72 spectral elements of polynomial degree $N = 4$: (a) spectral element mesh (modified mesh) and (b) close-up details of near the bump: spectral elements with GL grid.

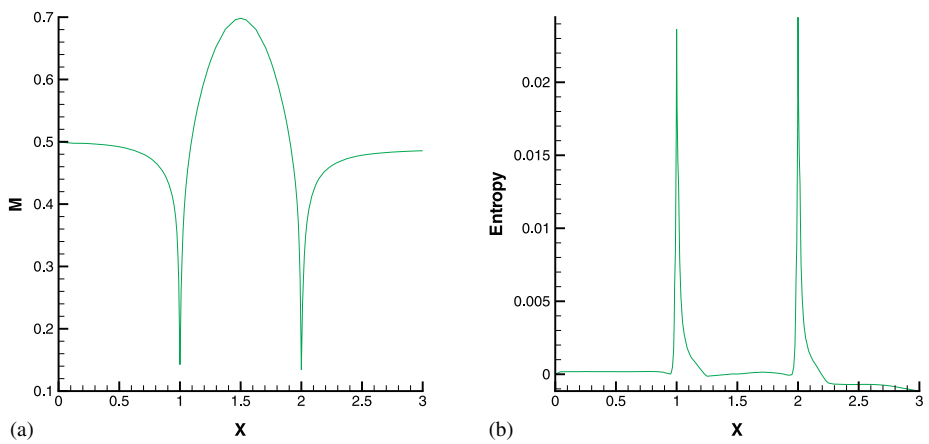

Figure 13. (a) The Mach number and (b) entropy distribution for the subsonic flow on a refined mesh.

DOI: 10.1002/fld

pronounced and the flow almost retains its inflow Mach number after the bump. The entropy change remains very small over the bump and the artificial entropy increase is restricted to the location of the stagnation points. Note that the deteriorating influence of the stagnation points is a result of the fact that a fully C^0 nodal approximation was used in this work. Ways to reduce (or even avoid) the influence of the stagnation points are the use of a staggered spectral element grid as described by Kopriva [39] or the use of a discontinuous spectral element formulation [40, 41].

6.2.3. Results for transonic flow. To investigate the transonic flow over a bump, the geometry is the same as that for the transonic flow problems described by Spekreijse [42] and Rizzi and Viviand [43].

As in the subsonic case, the chord length of the bump is $c=1$. The length of the channel, however, is 5 times the chord length and the height is set at 2.073 times the chord length. The height of the bump is 4.2% of the chord length. The mesh used for this test case is shown in Figure 14. The polynomial degree is $N=5$, whereas the integration order is $P=6$.

In Figure 15, the Mach contours at an inflow Mach number of $M=0.85$ and a time step of $\Delta t=0.075$ are compared with the finite volume results produced by Spekreijse [42].

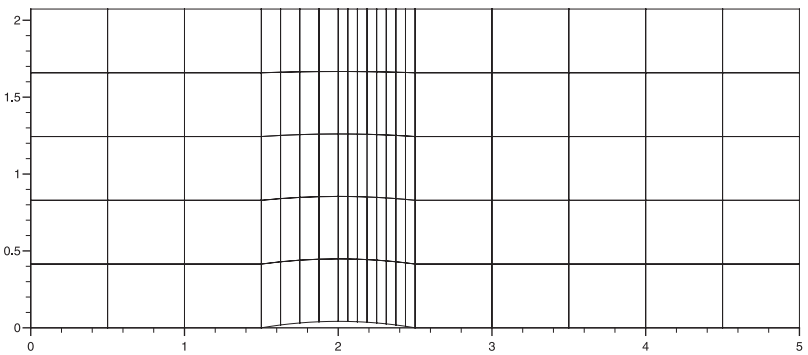

Figure 14. The mesh used for the transonic test case. The height of the bump is 4.2% of the chord length and 100 elements are used.

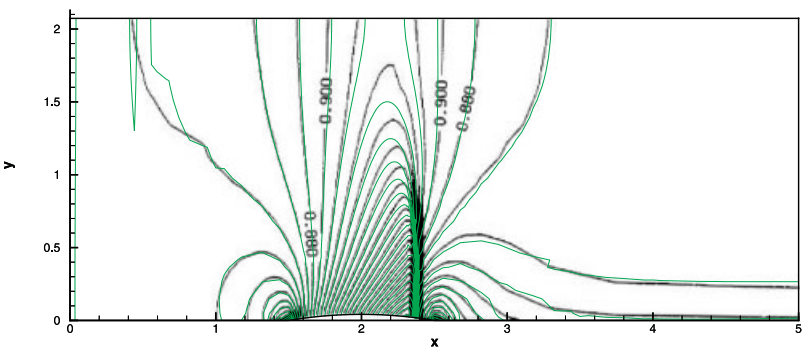

Figure 15. Comparison of the iso-Mach lines for transonic flow, $M=0.85$, obtained by LSQSEM (green) and finite volume method by Spekreijse [42] (black).

DOI: 10.1002/fld

The shock is positioned at approximately 86% of the bump with the Mach number just upstream of the shock being $M \approx 1.32$. These results are quantitatively in agreement with the finite volume results obtained by Spekreijse. In Figure 16, the Mach number distribution along the lower wall of the channel is shown. The shock is well captured and the Mach number drops from approximately 1.32 to 0.8 through the shock. This shock strength agrees with analytical shock relations, assuming a normal shock at the bump

$$M_2 = \sqrt{\frac{2+(\gamma-1)M_1^2}{1+2\gamma M_1^2-\gamma}}, \quad \text{so} \quad M_1 = 1.32 \quad \Longrightarrow \quad M_2 \approx 0.78 \tag{27}$$

6.2.4. Results for supersonic flow. The geometry used for the supersonic test case is similar to that considered for the subsonic flow test case. The only difference is the height of the bump which is 4% of the chord length for this test case. The mesh has a total of 120 elements as can be seen in Figure 17.

At inflow, the density is set to $\rho = 1.4$ and the pressure to $p = 1$. The Mach number of the flow at the inlet boundary is $M = 1.4$.

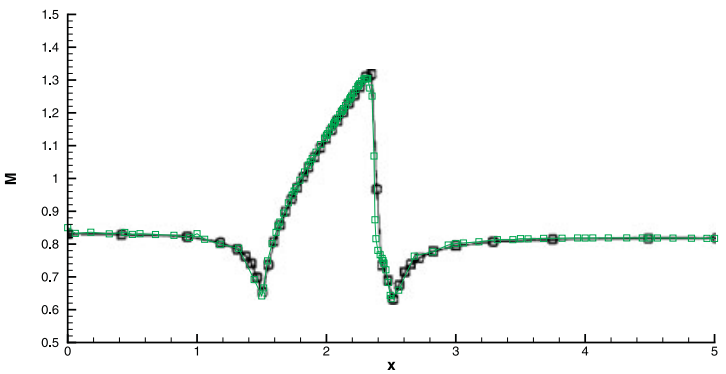

Figure 16. Comparison of the Mach number along the lower wall of the channel for a $M = 0.85$ flow with a 4.2% bump using a time step of $\Delta t = 0.075$ between LSQSEM solution (green line) and the finite volume results obtained by Spekreijse [42] (black line).

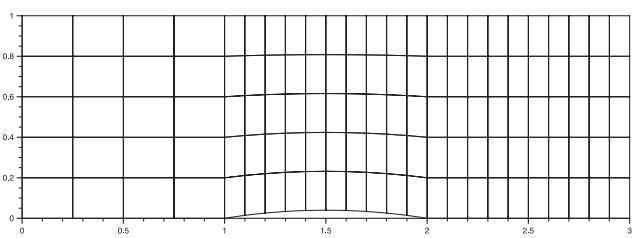

Figure 17. The mesh used for the supersonic test case. The height of the bump is 4% of the chord length and 120 elements are used.

DOI: 10.1002/fld

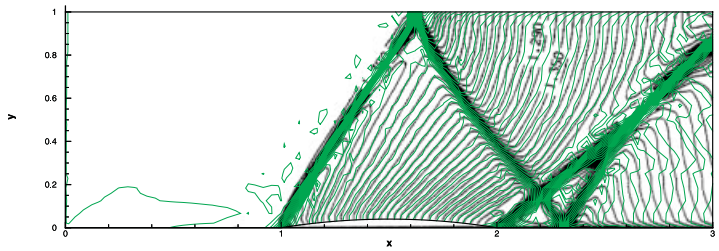

Figure 18. Iso-Mach lines and shock structure obtained by LSQSEM (green) and finite volume method by Spekreijse [42].

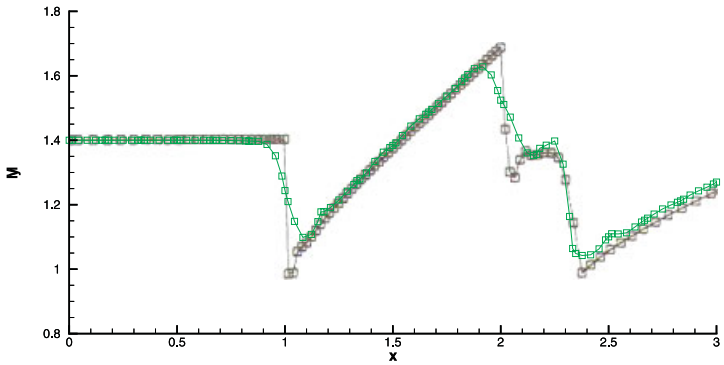

Figure 19. Comparison of the Mach number along the lower wall of the channel for a $M = 1.4$ between LSQSEM (green line) and the finite volume method by Spekreijse [42].

At the leading edge of the bump, a shock develops and runs into the domain until it is reflected by the upper wall. At the trailing edge also a shock originates at a slightly smaller angle than the shock at the leading edge. In the region behind the bump, the two shocks collide and then merge into a single shock. The iso-Mach contours for this test case are shown in Figure 18 together with the results obtained by Spekreijse [42]. This figure reveals that the shock structures over the bump agree.

The Mach number distribution along the lower wall is shown in Figure 19.

7. CONCLUSIONS

This paper described the least-squares spectral element formulation in which time stepping was used to reach steady-state solutions. The time integration method provides artificial diffusion which suppresses the oscillations in the vicinity of discontinuities. The time step should be chosen small enough to capture the large gradients in the flow and to avoid a dominant influence on the advection speeds.

The method was applied to inviscid, compressible flows governed by the Euler equations. For the wedge problem, it is demonstrated that a formulation in terms of conserved variables leads to

DOI: 10.1002/fld

the correct shock position, whereas a formulation in terms of primitive variables yields a shock position that deviates from the correct shock position.

For the subsonic flow over a circular bump, the influence of the time step, boundary weighing and the grid has been assessed to resolve the stagnation points at the leading and trailing edges of the bump. The entropy should be constant in this test case. By taking a smaller time step, different boundary weights or by refining the mesh around the stagnation points, the influence of these stagnation points on the solution in the interior of the computational domain is reduced.

In the transonic and supersonic test cases, over a circular bump shocks develop. Direct comparison with results from literature demonstrates that the LSQSEM method is capable of solving these types of flow problems.

APPENDIX A: LINEARIZED EULER

The two-dimensional Euler equations in conservation form are given by

$$\mathbf{U}_t+\mathbf{F}(\mathbf{U})_x+\mathbf{G}(\mathbf{U})_y=\mathbf{0}$$

Here $\mathbf{U}=(\rho,\rho u,\rho v,\rho E)^T$ is a vector containing the conserved variables and the flux vectors $\mathbf{F}$ and $\mathbf{G}$ are

$$\mathbf{F}=\begin{bmatrix}\rho u\\ \rho u^2+p\\ \rho uv\\ \rho uH\end{bmatrix},\quad \mathbf{G}=\begin{bmatrix}\rho v\\ \rho uv\\ \rho v^2+p\\ \rho vH\end{bmatrix} \tag{A1}$$

The total energy E and total enthalpy H are given by

$$\rho E=\frac{p}{\gamma-1}+\frac{1}{2}\rho(u^2+v^2),\quad H=E+\frac{p}{\rho} \tag{A2}$$

The Euler equation in non-conservation form but in terms of the conserved quantities is given by

$$\mathbf{U}_t+\mathbf{A}(\mathbf{U})\mathbf{U}_x+\mathbf{B}(\mathbf{U})\mathbf{U}_y=\mathbf{0} \tag{A3}$$

where the Jacobian matrices $\mathbf{A}(\mathbf{U})$ and $\mathbf{B}(\mathbf{U})$ are given by

$$\mathbf{A}=\begin{bmatrix}A_{00} & A_{01} & A_{02} & A_{03}\\ A_{10} & A_{11} & A_{12} & A_{13}\\ A_{20} & A_{21} & A_{22} & A_{23}\\ A_{30} & A_{31} & A_{32} & A_{33}\end{bmatrix} \tag{A4}$$

$$\mathbf{B}=\begin{bmatrix}B_{00} & B_{01} & B_{02} & B_{03}\\ B_{10} & B_{11} & B_{12} & B_{13}\\ B_{20} & B_{21} & B_{22} & B_{23}\\ B_{30} & B_{31} & B_{32} & B_{33}\end{bmatrix} \tag{A5}$$

DOI: 10.1002/fld

with

$$A_{00}=0,\quad A_{01}=1,\quad A_{02}=0,\quad A_{03}=0$$

$$A_{10}=\frac{(\gamma-3)}{2}\frac{(\rho u)^2}{\rho^2}+\frac{(\gamma-1)}{2}\frac{(\rho v)^2}{\rho^2}$$

$$A_{11}=-(\gamma-3)\frac{(\rho u)}{\rho},\quad A_{12}=-(\gamma-1)\frac{(\rho v)}{\rho},\quad A_{13}=(\gamma-1)$$

$$A_{20}=-\frac{(\rho u)(\rho v)}{\rho^2},\quad A_{21}=\frac{(\rho v)}{\rho},\quad A_{22}=\frac{(\rho u)}{\rho},\quad A_{23}=0$$

$$A_{30}=-\gamma\frac{(\rho u)(\rho E)}{\rho^2}+(\gamma-1)\frac{(\rho u)^3}{\rho^3}+(\gamma-1)\frac{(\rho u)(\rho v)^2}{\rho^3}$$

$$A_{31}=\gamma\frac{(\rho E)}{\rho}-3\frac{(\gamma-1)}{2}\frac{(\rho u)^2}{\rho^2}-\frac{(\gamma-1)}{2}\frac{(\rho v)^2}{\rho^2},\quad A_{32}=-(\gamma-1)\frac{(\rho u)(\rho v)}{\rho^2},\quad A_{33}=\gamma\frac{(\rho u)}{\rho}$$

$$B_{00}=0,\quad B_{01}=0,\quad B_{02}=1,\quad B_{03}=0$$

$$B_{10}=-\frac{(\rho u)(\rho v)}{\rho^2},\quad B_{11}=\frac{(\rho v)}{\rho},\quad B_{12}=\frac{(\rho u)}{\rho},\quad B_{13}=0$$

$$B_{20}=\frac{(\gamma-3)}{2}\frac{(\rho v)^2}{\rho^2}+\frac{(\gamma-1)}{2}\frac{(\rho u)^2}{\rho^2},\quad B_{21}=-(\gamma-1)\frac{(\rho u)}{\rho},\quad B_{22}=-(\gamma-3)\frac{(\rho v)}{\rho},\quad B_{23}=(\gamma-1)$$

$$B_{30}=-\gamma\frac{(\rho v)(\rho E)}{\rho^2}+(\gamma-1)\frac{(\rho v)^3}{\rho^3}+(\gamma-1)\frac{(\rho v)(\rho u)^2}{\rho^3},\quad B_{31}=-(\gamma-1)\frac{(\rho v)(\rho u)}{\rho^2}$$

$$B_{32}=\gamma\frac{(\rho E)}{\rho}-3\frac{(\gamma-1)}{2}\frac{(\rho v)^2}{\rho^2}-\frac{(\gamma-1)}{2}\frac{(\rho u)^2}{\rho^2},\quad B_{33}=\gamma\frac{(\rho v)}{\rho}$$

Linearization of these non-linear expressions with respect to the primitive variable $(\rho, \rho u, \rho v, \rho E)$ gives the linearized operator $\mathbf{L}$.

Therefore, the linearized Jacobian matrices for the Euler equations in terms of conserved quantities can be expressed as

$$\mathbf{U}_t+\mathbf{L}_0\mathbf{U}+\mathbf{L}_1\mathbf{U}_x+\mathbf{L}_2\mathbf{U}_y=\mathbf{0}$$

where

$$\mathbf{L}_0=\begin{bmatrix} L_0^{00} & L_0^{01} & L_0^{02} & L_0^{03} \\ L_0^{10} & L_0^{11} & L_0^{12} & L_0^{13} \\ L_0^{20} & L_0^{21} & L_0^{22} & L_0^{23} \\ L_0^{30} & L_0^{31} & L_0^{32} & L_0^{33} \end{bmatrix} \tag{A6}$$

with

$$L_0^{00}=0,\quad L_0^{01}=0,\quad L_0^{02}=0,\quad L_0^{03}=0$$

DOI: 10.1002/fld

$$L_0^{01}=(3-\gamma)\left[\frac{(\rho u)_0^2}{\rho_0^3}\frac{\partial\rho_0}{\partial x}-\frac{(\rho u)_0}{\rho_0^2}\frac{\partial(\rho u)_0}{\partial x}\right]+(1-\gamma)\left[\frac{(\rho v)_0^2}{\rho_0^3}\frac{\partial\rho_0}{\partial x}-\frac{(\rho v)_0}{\rho_0^2}\frac{\partial(\rho v)_0}{\partial x}\right]$$

$$+\left[2\frac{(\rho u)_0(\rho v)_0}{\rho_0^3}\frac{\partial\rho_0}{\partial y}-\frac{(\rho u)_0}{\rho_0^2}\frac{\partial(\rho v)_0}{\partial y}-\frac{(\rho v)_0}{\rho_0^2}\frac{\partial(\rho u)_0}{\partial y}\right]$$

$$L_0^{11}=(3-\gamma)\left[\frac{1}{\rho_0}\frac{\partial(\rho u)_0}{\partial x}-\frac{(\rho u)_0}{\rho_0^2}\frac{\partial\rho_0}{\partial x}\right]+\left[\frac{1}{\rho_0}\frac{\partial(\rho v)_0}{\partial y}-\frac{(\rho v)_0}{\rho_0^2}\frac{\partial\rho_0}{\partial y}\right]$$

$$L_0^{12}=(1-\gamma)\left[\frac{1}{\rho_0}\frac{\partial(\rho v)_0}{\partial x}-\frac{(\rho v)_0}{\rho_0^2}\frac{\partial\rho_0}{\partial x}\right]+\left[\frac{1}{\rho_0}\frac{\partial(\rho u)_0}{\partial y}-\frac{(\rho u)_0}{\rho_0^2}\frac{\partial\rho_0}{\partial y}\right]$$

$$L_0^{13}=0$$

$$L_0^{20}=\left[2\frac{(\rho u)_0(\rho v)_0}{\rho_0^3}\frac{\partial\rho_0}{\partial x}-\frac{(\rho u)_0}{\rho_0^2}\frac{\partial(\rho v)_0}{\partial x}-\frac{(\rho v)_0}{\rho_0^2}\frac{\partial(\rho u)_0}{\partial x}\right]$$

$$+(1-\gamma)\left[\frac{(\rho u)_0^2}{\rho_0^3}\frac{\partial\rho_0}{\partial y}-\frac{(\rho u)_0}{\rho_0^2}\frac{\partial(\rho u)_0}{\partial y}\right]+(3-\gamma)\left[\frac{(\rho v)_0^2}{\rho_0^3}\frac{\partial\rho_0}{\partial y}-\frac{(\rho v)_0}{\rho_0^2}\frac{\partial(\rho v)_0}{\partial y}\right]$$

$$L_0^{21}=\left[\frac{1}{\rho_0}\frac{\partial(\rho v)_0}{\partial x}-\frac{(\rho v)_0}{\rho_0^2}\frac{\partial\rho_0}{\partial x}\right]+(1-\gamma)\left[\frac{1}{\rho_0}\frac{\partial(\rho u)_0}{\partial y}-\frac{(\rho u)_0}{\rho_0^2}\frac{\partial\rho_0}{\partial y}\right]$$

$$L_0^{22}=\left[\frac{1}{\rho_0}\frac{\partial(\rho u)_0}{\partial x}-\frac{(\rho u)_0}{\rho_0^2}\frac{\partial\rho_0}{\partial x}\right]+(3-\gamma)\left[\frac{1}{\rho_0}\frac{\partial(\rho v)_0}{\partial y}-\frac{(\rho v)_0}{\rho_0^2}\frac{\partial\rho_0}{\partial y}\right]$$

$$L_0^{23}=0$$

$$L_0^{30}=\gamma\left[2\frac{(\rho u)_0(\rho E)_0}{\rho_0^3}\frac{\partial\rho_0}{\partial x}-\frac{(\rho u)_0}{\rho_0^2}\frac{\partial(\rho E)_0}{\partial x}-\frac{(\rho E)_0}{\rho_0^2}\frac{\partial(\rho u)_0}{\partial x}\right]$$

$$+3(1-\gamma)\left[\frac{(\rho u)_0^3}{\rho_0^4}\frac{\partial\rho_0}{\partial x}-\frac{(\rho u)_0^2}{\rho_0^3}\frac{\partial(\rho u)_0}{\partial x}\right]$$

$$+(1-\gamma)\left[3\frac{(\rho u)_0(\rho v)_0^2}{\rho_0^4}\frac{\partial\rho_0}{\partial x}-2\frac{(\rho u)_0(\rho v)_0}{\rho_0^3}\frac{\partial(\rho v)_0}{\partial x}-\frac{(\rho v)_0^2}{\rho_0^3}\frac{\partial(\rho u)_0}{\partial x}\right]$$

DOI: 10.1002/fld

$$+\gamma\left[2\frac{(\rho v)_0(\rho E)_0}{\rho_0^3}\frac{\partial\rho_0}{\partial y}-\frac{(\rho v)_0}{\rho_0^2}\frac{\partial(\rho E)_0}{\partial y}-\frac{(\rho E)_0}{\rho_0^2}\frac{\partial(\rho v)_0}{\partial y}\right]$$

$$+3(1-\gamma)\left[\frac{(\rho v)_0^3}{\rho_0^4}\frac{\partial\rho_0}{\partial y}-\frac{(\rho v)_0^2}{\rho_0^3}\frac{\partial(\rho v)_0}{\partial y}\right]$$

$$+(1-\gamma)\left[3\frac{(\rho v)_0(\rho u)_0^2}{\rho_0^4}\frac{\partial\rho_0}{\partial y}-2\frac{(\rho v)_0(\rho u)_0}{\rho_0^3}\frac{\partial(\rho u)_0}{\partial y}-\frac{(\rho u)_0^2}{\rho_0^3}\frac{\partial(\rho v)_0}{\partial y}\right]$$

$$L_0^{31}=\gamma\left[\frac{1}{\rho_0}\frac{\partial(\rho E)_0}{\partial x}-\frac{(\rho E)_0}{\rho_0^2}\frac{\partial\rho_0}{\partial x}\right]$$

$$+3(1-\gamma)\left[\frac{(\rho u)_0}{\rho_0^2}\frac{\partial(\rho u)_0}{\partial x}-\frac{(\rho u)_0^2}{\rho_0^3}\frac{\partial\rho_0}{\partial x}\right]+(1-\gamma)\left[\frac{(\rho v)_0}{\rho_0^2}\frac{\partial(\rho v)_0}{\partial x}-\frac{(\rho v)_0^2}{\rho_0^3}\frac{\partial\rho_0}{\partial x}\right]$$

$$+(1-\gamma)\left[\frac{(\rho v)_0}{\rho_0^2}\frac{\partial(\rho u)_0}{\partial y}+\frac{(\rho u)_0}{\rho_0^2}\frac{\partial(\rho v)_0}{\partial y}-2\frac{(\rho v)_0(\rho u)_0}{\rho_0^3}\frac{\partial\rho_0}{\partial y}\right]$$

$$L_0^{32}=\gamma\left[\frac{1}{\rho_0}\frac{\partial(\rho E)_0}{\partial y}-\frac{(\rho E)_0}{\rho_0^2}\frac{\partial\rho_0}{\partial y}\right]+3(1-\gamma)\left[\frac{(\rho v)_0}{\rho_0^2}\frac{\partial(\rho v)_0}{\partial y}-\frac{(\rho v)_0^2}{\rho_0^3}\frac{\partial\rho_0}{\partial y}\right]$$

$$+(1-\gamma)\left[\frac{(\rho u)_0}{\rho_0^2}\frac{\partial(\rho u)_0}{\partial y}-\frac{(\rho u)_0^2}{\rho_0^3}\frac{\partial\rho_0}{\partial y}\right]$$

$$+(1-\gamma)\left[\frac{(\rho u)_0}{\rho_0^2}\frac{\partial(\rho v)_0}{\partial x}+\frac{(\rho v)_0}{\rho_0^2}\frac{\partial(\rho u)_0}{\partial x}-2\frac{(\rho u)_0(\rho v)_0}{\rho_0^3}\frac{\partial\rho_0}{\partial x}\right]$$

$$L_0^{33}=\gamma\left[\frac{1}{\rho_0}\frac{\partial(\rho u)_0}{\partial x}-\frac{(\rho u)_0}{\rho_0^2}\frac{\partial\rho_0}{\partial x}\right]+\gamma\left[\frac{1}{\rho_0}\frac{\partial(\rho v)_0}{\partial y}-\frac{(\rho v)_0}{\rho_0^2}\frac{\partial\rho_0}{\partial y}\right]$$

And

$$\mathbf{L}_1=\begin{bmatrix}L_1^{00} & L_1^{01} & L_1^{02} & L_1^{03}\\ L_1^{10} & L_1^{11} & L_1^{12} & L_1^{13}\\ L_1^{20} & L_1^{21} & L_1^{22} & L_1^{23}\\ L_1^{30} & L_1^{31} & L_1^{32} & L_1^{33}\end{bmatrix} \tag{A7}$$

with

$$L_1^{00}=0,\quad L_1^{01}=1,\quad L_1^{02}=0,\quad L_1^{03}=0$$

$$L_1^{10}=\frac{(\gamma-3)}{2}\frac{(\rho u)_0^2}{\rho_0^2}+\frac{(\gamma-1)}{2}\frac{(\rho v)_0^2}{\rho_0^2}$$

DOI: 10.1002/fld

$$L_1^{11}=(3-\gamma)\frac{(\rho u)_0}{\rho_0},\quad L_1^{12}=(1-\gamma)\frac{(\rho v)_0}{\rho_0},\quad L_1^{13}=(\gamma-1)$$

$$L_1^{20}=-\frac{(\rho u)_0(\rho v)_0}{\rho_0^2},\quad L_1^{21}=\frac{(\rho v)_0}{\rho_0},\quad L_1^{22}=\frac{(\rho u)_0}{\rho_0},\quad L_1^{23}=0$$

$$L_1^{30}=(\gamma-1)\left[\frac{(\rho u)_0^3}{\rho_0^3}+\frac{(\rho u)_0(\rho v)_0^2}{\rho_0^3}\right]-\gamma\frac{(\rho u)_0(\rho E)_0}{\rho_0^2}$$

$$L_1^{31}=\gamma\frac{(\rho E)_0}{\rho_0}+\frac{(1-\gamma)}{2}\left[3\frac{(\rho u)_0^2}{\rho_0^2}+\frac{(\rho v)_0^2}{\rho_0^2}\right],\quad L_1^{32}=(1-\gamma)\frac{(\rho u)_0(\rho v)_0}{\rho_0^2},\quad L_1^{33}=\gamma\frac{(\rho u)_0}{\rho_0}$$

And

$$\mathbf{L}_2=\begin{bmatrix}L_2^{00} & L_2^{01} & L_2^{02} & L_2^{03}\\ L_2^{10} & L_2^{11} & L_2^{12} & L_2^{13}\\ L_2^{20} & L_2^{21} & L_2^{22} & L_2^{23}\\ L_2^{30} & L_2^{31} & L_2^{32} & L_2^{33}\end{bmatrix} \tag{A8}$$

with

$$L_2^{00}=0,\quad L_2^{01}=0,\quad L_2^{02}=1,\quad L_2^{03}=0$$

$$L_2^{10}=-\frac{(\rho u)_0(\rho v)_0}{\rho_0^2},\quad L_2^{11}=\frac{(\rho v)_0}{\rho_0},\quad L_2^{12}=\frac{(\rho u)_0}{\rho_0},\quad L_2^{13}=0$$

$$L_2^{20}=\frac{(\gamma-1)}{2}\frac{(\rho u)_0^2}{\rho_0^2}+\frac{(\gamma-3)}{2}\frac{(\rho v)_0^2}{\rho_0^2}$$

$$L_2^{21}=(1-\gamma)\frac{(\rho u)_0}{\rho_0},\quad L_2^{22}=(3-\gamma)\frac{(\rho v)_0}{\rho_0},\quad L_2^{23}=(\gamma-1)$$

$$L_2^{30}=(\gamma-1)\left[\frac{(\rho v)_0^3}{\rho_0^3}+\frac{(\rho v)_0(\rho u)_0^2}{\rho_0^3}\right]-\gamma\frac{(\rho v)_0(\rho E)_0}{\rho_0^2},\quad L_2^{31}=(1-\gamma)\frac{(\rho v)_0(\rho u)_0}{\rho_0^2}$$

$$L_2^{32}=\gamma\frac{(\rho E)_0}{\rho_0}+\frac{(1-\gamma)}{2}\left[3\frac{(\rho v)_0^2}{\rho_0^2}+\frac{(\rho u)_0^2}{\rho_0^2}\right],\quad L_2^{33}=\gamma\frac{(\rho v)_0}{\rho_0}$$

ACKNOWLEDGEMENTS

The authors wish to thank the referees for their valuable contribution to this paper.

REFERENCES

1. Lax PD. Weak solutions of nonlinear hyperbolic equations and their numerical calculation. *Communications on Pure and Applied Mathematics* 1954; **7**:159–193.

DOI: 10.1002/fld

2. Hirsch C. *Numerical Computation of Internal and External Flows—Vol. 2*: *Computational Methods for Inviscid and Viscous Flows*. Wiley: New York, 1990.
3. LeVeque RJ. *Finite Volume Methods for Hyperbolic Problems*. Cambridge University Press: Cambridge, 2002.
4. Toro EF. *Riemann Solvers and Numerical Methods for Fluid Dynamics—A Practical Introduction*. Springer: Berlin, Heidelberg, New York, 1999.
5. Chang CL, Nelson JJ. Least-squares finite element method for the Stokes problem with zero residual of mass conservation. *SIAM Journal on Numerical Analysis* 1997; **34**(2):480–489.
6. Deang JM, Gunzburger MD. Issues related to least-squares finite element methods for the Stokes equations. *SIAM Journal on Scientific Computing* 1998; **20**(3):878–906.
7. Proot MMJ, Gerritsma MI. Mass and momentum conservation of the least-squares spectral element method for the Stokes problem. *Journal of Scientific Computing* 2005; **27**:389–401.
8. Heys JJ, Lee E, Manteuffel TA, McCormick SF. On mass-conserving least-squares methods. *Journal of Scientific Computing* 2006; **28**(5):1675–1693.
9. Houston P, Senior B, Süli E. Sobolev regularity estimation for *hp*-adaptive finite element methods. *Technical Report NA-02-02*, University of Oxford, 2002.
10. Gottlieb D, Hesthaven JS. Spectral methods for hyperbolic problems. *Journal of Computational and Applied Mathematics* 2001; **128**:83–131.
11. Guo B-Y, Ma H-P, Tadmor E. Spectral vanishing viscosity method for nonlinear conservation laws. *SIAM Journal on Numerical Analysis* 2001; **39**(4):1254–1268.
12. Maday Y, Tadmor E. Analysis of the spectral vanishing viscosity method for periodic conservation laws. *SIAM Journal on Numerical Analysis* 1989; **26**(4):854–870.
13. Tadmor E. Convergence of spectral methods for nonlinear conservation laws. *SIAM Journal on Numerical Analysis* 1989; **26**(1):30–44.
14. Jiang B-N. On the least-squares method. *Computer Methods in Applied Mechanics and Engineering* 1998; **152**(1–2):239–257.
15. Guermond J-L. A finite element technique for solving first order PDE's in L^p. *SIAM Journal on Numerical Analysis* 2004; **42**(2):714–737.
16. Guermond J-L, Popov B. Linear advection with ill-posed boundary conditions via L^1-minimization. *International Journal of Numerical Analysis and Modeling* 2007; **4**:39–47.
17. De Sterck H, Manteuffel TA, McCormick SF. Least-squares finite element methods and algebraic multigrid solvers for linear hyperbolic pdes. *SIAM Journal on Scientific Computing* 2004; **26**:31–54.
18. De Sterck H, Manteuffel TA, McCormick SF, Olson L. Numerical conservation properties of h(div)-conforming least-squares finite element methods for the Burgers equation. *SIAM Journal on Scientific Computing* 2005; **26**(5):1573–1597.
19. De Maerschalck B, Gerritsma MI. Least-squares spectral element method with entropy inequality constraint. In *European Conference on Computational Fluid Dynamics*, *ECCOMAS 2006*, Egmond aan Zee, Wesseling P, Oñate E, Périaux J (eds.), 2006.
20. De Maerschalck B, Gerritsma MI, Proot MMJ. Space–time least-squares spectral elements for convection dominated unsteady flows. *AIAA Journal* 2006; **44**(3):558–565.
21. De Maerschalck B, Gerritsma MI. The use of Chebyshev polynomials in the space–time least squares spectral element method. *Numerical Algorithms* 2005; **38**(1):173–196.
22. De Maerschalck B, Gerritsma MI. Least-squares spectral element method for non-linear hyperbolic differential equations. *Journal of Computational and Applied Mathematics* 2007. DOI: 10.1016/j.cam.2006.03.060.
23. Heinrichs W. Spectral collocation schemes on the unit disc. *Journal of Computational Physics* 2004; **199**:66–86.
24. Heinrichs W. Least-squares spectral collocation for the Navier–Stokes equations. *Journal of Scientific Computing* 2004; **21**:81–90.
25. Taghaddosi F, Habashi WG, Guèvremont G, Ait-Ali-Yahia D. An adaptive least-squares method for the compressible Euler equations. *AIAA Paper 97-2097*, 1997.
26. Taghaddosi F, Habashi WG, Guèvremont G, Ait-Ali-Yahia D. An adaptive approach least-squares method for the compressible Euler equations. *International Journal for Numerical Methods in Fluids* 1999; **31**:1121–1139.
27. Bochev PB, Gunzburger MD. Finite element methods of least-squares type. *SIAM Review* 1998; **40**(4):789–837.
28. van der Bas R. Least-squares spectral element method for 2-D hyperbolic systems of equations. *Technical Report Stagiaire Report 2007-07*, Von Karman Institute for Fluid Dynamics, Belgium, 2007.
29. Hoitinga W, De Groot R, Kwakkel M, Gerritsma MI. Direct minimization of the least-squares spectral element functional—Part I: direct solver. *Journal of Computational Physics* 2008; **227**:2411–2429.

30. Tadmor E. Entropy stability theory for difference approximations of nonlinear conservation laws and related time-dependent problems. *Acta Numerica* 2003; **12**:451–512.
31. Evans LC. Entropy and partial differential equations. *Technical Report*, Department of Mathematics, UC Berkeley, 2001.
32. Ball JM. Singularities and computation of minimizers for variational problems. In *Foundations of Computational Mathematics*, DeVore RA, Iserles A, Süli E (eds), *London Mathematical Society Lecture Notes Series 284*, Cambridge University Press: Cambridge, U.K., 2001. ISBN: 0521003490.
33. Oldenziel G. Least-squares spectral element method for 1D hyperbolic differential equations—evaluation of two time stepping methods. *Technical Report, MSc Thesis*, Faculty of Aerospace Engineering, TU Delft, 2007.
34. Canuto C, Hussaini MY, Quarteroni A, Zang TA. *Spectral Methods in Fluid Dynamics*. Springer Series in Computational Physics. Springer: Berlin, 1988.
35. Deville MO, Fisher PF, Mund EH. *High-order Methods for Incompressible Fluid Flow*. Cambridge University Press: Cambridge, 2002.
36. Karniadakis GEM, Sherwin SJ. *Spectral h/p Element Methods for CFD*. Oxford University Press: Oxford, 1999.
37. De Maerschalck B, Gerritsma MI. Higher-order Gauss–Lobatto integration for non-linear hyperbolic equations. *Journal of Scientific Computing* 2006; **27**(1–3):201–214.
38. Gordon WJ, Hall CA. Transfinite element methods—blending-function interpolation over arbitrary curved element domains. *Numerische Mathematik* 1973; **21**(2):109–129.
39. Kopriva DA. A staggered-grid multidomain spectral method for the compressible Navier–Stokes equations. *Journal of Computational Physics* 1998; **143**(1):125–158.
40. Gerritsma MI. Direct minimization of the discontinuous least-squares spectral element method for viscoelastic fluids. *Journal of Scientific Computing* 2006; **27**(1–3):245–256.
41. Gerritsma MI, Proot MMJ. Analysis of a discontinuous least squares spectral element method. *Journal of Scientific Computing* 2002; **17**:297–306.
42. Spekreijse SP. *Multigrid Solution of the Steady Euler Equations*. CWI Tracts, vol. 46. Stichting Mathematisch Centrum: Amsterdam, 1988.
43. Rizzi A, Viviand H. *Numerical Methods for the Computation of Inviscid Flows with Shock Waves*. Vieweg: Braunschweig, 1981.

DOI: 10.1002/fld